Shock wave–bubble interaction near soft and rigid boundaries during lithotripsy: numerical analysis by the improved ghost fluid method

Kazumichi Kobayashi[1], Tetsuya Kodama[2] and Hiroyuki Takahira[3]

[1]Division of Mechanical and Space Engineering, Faculty of Engineering, Hokkaido University, Kita 13, Nishi 8, Kita-ku, Sapporo, Hokkaido 060-8628, Japan
[2]Department of Biomedical Engineering, Graduate School of Biomedical Engineering, Tohoku University, 2-1 Seiryo-machi, Aoba-ku, Sendai 980-8575, Japan
[3]Department of Mechanical Engineering, Graduate School of Engineering, Osaka Prefecture University, 1-1 Gakuen-cho, Naka-ku, Sakai 599-8531, Japan

E-mail: kobakazu@eng.hokudai.ac.jp

Abstract. In the case of extracorporeal shock wave lithotripsy (ESWL), a shock wave–bubble interaction inevitably occurs near the focusing point of stones, resulting in stone fragmentation and subsequent tissue damage. Because shock wave–bubble interactions are high-speed phenomena occurring in the tissue consisting of various media with different acoustic impedance values, numerical analysis is an effective method for elucidating the mechanism of these interactions. However, the mechanism has not been examined in detail because, at present, numerical simulations capable of incorporating the acoustic impedance of various tissues do not exist. Here, we show that the improved ghost fluid method (IGFM) can treat the shock wave–bubble interactions in various media. Nonspherical bubble collapse near a rigid or soft tissue boundary (stone, liver, gelatin, and fat) was analyzed. The reflection wave of an incident shock wave at a tissue boundary was the primary cause for the acceleration or deceleration of bubble collapse. The impulse that was obtained from the temporal evolution of pressure created by the bubble collapse increased the downward velocity of the boundary and caused subsequent boundary deformation. Results of this study showed that IGFM is a useful method for analyzing the shock wave–bubble interaction near various tissues with different acoustic impedance.

1. Introduction

Extracorporeal shock wave lithotripsy (ESWL) is currently the only noninvasive method for removing calculi in human bodies (Lingeman *et al* 2009), accounting for 70% of the treatment of the upper urinary tract calculi (Semins *et al* 2008). In ESWL, converging shock waves generated outside a patient body in electrohydraulic, piezoelectric, and electromagnetic ways are focused on a target to be operated on inside the body. Pressure is induced by a converging shock wave consisting of positive pulses accompanied with negative pulses. In a typical ESWL (Loske 2010), the positive pulse has a height of 150 MPa, a rise time of 10 ns, and a duration ranging from 0.5 to 3 μs, whereas the subsequent negative pulse has a depth of -25 MPa and a duration ranging from 2 to 20 μs, causing the formation of bubbles in the liquid, which successively grow and collapse, i.e., cavitation.

The converging shock waves are applied to the target, with repetition frequencies in the range of 0.5–2 Hz (e.g. Yilmaz *et al* 2005). The cavtaion nuclei or grown bubbles by the converging shock waves inevitably interact with the subsequent shock waves. The presence of bubbles not only affects the efficiency of ESWL operations but also causes tissue damage in the human body (Kodama and Takayama 1998). Therefore, the elucidation of the interaction between the bubbles and the shock waves is crucial for enhancing the efficiency and for understanding the region and degree of tissue damage as well as for devising treatment plans (Tham *et al* 2007). A number of investigations of the shock wave–bubble interaction have been made experimentally. For example, Kodama and Takayama (1998) observed the collapse and subsequent liquid-jet formation of a single air bubble attached to gelatin, extirpated livers, and abdominal aortas as tissue models, and they demonstrated that tissue damage was caused by the liquid-jet impingement. Loske (2010) investigated the influence of acoustic cavitation on stone fragmentation and clarified that energy density is the key parameter of a stone fragment.

However, in all the experiments, the shock wave–bubble interaction is a high-speed phenomenon that is too fast to be captured clearly because of restrictions related to space and time resolutions in the observation facilities used.

The recent progress in computational fluid dynamics with the high resolutions in space and time is remarkable and makes it possible to clarify such a high-speed phenomenon. Thus far, the shock wave–bubble interaction has been studied with several numerical methods (Calvisi *et al* 2008, Freund *et al* 2009, Johnsen and Colonius 2008, 2009, Takahira *et al* 2008, 2009). Calvisi *et al* (2008) calculated the bubble collapse near a rigid boundary using the boundary integral method and clarified that the bubble collapse process with the formation of liquid jet depends on the distance of the bubble relative to the wall when the reflection of the incident wave is taken into account. Freund *et al* (2009) investigated the problem using the finite volume method. They found that the viscous resistance in tissues can significantly suppress the penetration of the liquid jet induced by the bubble collapse. In the simulation, the boundary is treated as a viscous fluid and there is no acoustic impedance mismatch at the tissue boundary. Johnsen and Colonius solved the shock-bubble interaction near a rigid boundary using the high-order scheme (Johnsen and Colonius 2006). They investigated the precision dynamics of bubble collapse near the boundary, e.g., the liquid jet formation during the bubble collapse, the water-hammer shock wave, and the precursor shock wave due to the liquid jet. Since the boundary was assumed to be rigid in the above works (Calvisi *et al* 2008, Johnsen and Colonius 2008, 2009), the deformation of the wall was not taken into account.

Takahira *et al* (2008, 2009) investigated the shock-bubble interactions near a glass wall in mercury with an improved ghost fluid method. In the study, the wall was treated as a stiffened fluid in which the deformation of the wall and the acoustic impedance of the wall material were taken into consideration. The ghost fluid method (GFM) is capable of treating the discontinuity of physical quantities, e.g., density and entropy, at the gas–liquid interface using artificial cells (Fedkiw *et al* 1999). The GFM with the fully Eulerian scheme is sometimes unstable in the computation of compressible flows with a gas–liquid interface; unrealistic pressure oscillations occur near the gas–liquid interface and the solution diverges (Fedkiw 2002). This problem is caused by the large sensitivity of the scheme to numerical errors across the interface. To avoid these numerical errors, Takahira *et al* (2008, 2009) developed an improved GFM (IGFM) in which values in both regions of the interface are corrected using values at the neighboring nodes and the solution of the Riemann problem at the interface.

In the present study, we improved the ghost fluid method developed by Takahira *et al* (2008, 2009) to analyze the shock wave profile (figure 2) and to apply the method for the shock-bubble interaction near a tissue boundary. Thus the deformation of the tissue boundary and the reflection of the pressure wave on the boundary can be investigated in the present work. We clarify the deformation and collapse of a bubble near the soft or rigid tissue as well as the influence of impulsive pressures induced by bubble collapse on the tissue boundary. The numerical simulations are conducted for an axi-symmetric system. Although the present analysis is restricted to the axi-symmetric motion, the essence of the actual bubble collapse, such as the lifetime of a bubble near boundaries, the formation of a toroidal bubble, the generation of the shock wave from the collapsing bubble, and the deformation of the material boundaries, can also be included.

2. Numerical procedure

2.1. Governing equations and state equation

In the present analysis, the motions of three phases, namely, the gas inside a bubble, the liquid surrounding the bubble, and the material of the boundary are analyzed. The schematic model is shown in figure 1. The three phases are treated as immiscible compressible fluids. The governing equations for each fluid are a set of axi-symmetric Euler equations for the compressible flows:

$$\begin{pmatrix} \rho \\ \rho u \\ \rho v \\ E \end{pmatrix}_t + \begin{pmatrix} \rho u \\ \rho u^2 + p \\ \rho uv \\ (E+p)u \end{pmatrix}_r + \begin{pmatrix} \rho v \\ \rho uv \\ \rho v^2 + p \\ (E+p)v \end{pmatrix}_z = -\frac{1}{r}\begin{pmatrix} \rho u \\ \rho u^2 \\ \rho uv \\ (E+p)u \end{pmatrix}, \tag{1}$$

where t is the time, r and z are the radial and axial coordinates (the origin of each coordinate is the left lower edge of the system shown in figure 1), respectively, ρ is the density, u and v are the velocity components in the r- and z-directions, respectively, E ($=\rho[e+(u^2+v^2)/2]$) is the total energy per unit volume, where e is the internal energy per unit mass, and p is the pressure. Subscripts t, r, and z denote differentiation with respect to t, r, and z, respectively. Each line of equation 1 represents the conservation of the mass, the momentum in the r and z directions, and the energy, respectively. The third-order TVD Runge–Kutta scheme and the third-order ENO-LLF scheme (Shu *et al* 1989) are used for the time and space discretizations of (1), respectively.

We adopt the following stiffened gas equation of state for air within the bubble, water around it, and tissue materials (Saurel and Abgrall 1999):

$$p=(\gamma-1)\rho e-\gamma\Pi, \tag{2}$$

where γ and Π are the parameters characterizing the materials. The equation of state is needed to determine the relationship between the state variables: the density, internal energy, and pressure. The tissue material is thus treated as a compressible fluid. Sanurel and Abrall (1999) treated granite as a stiffened gas in their simulation. As discussed in Zukas *et al* (1982), a shock wave propagates in a solid material in a manner similar to that in the case of fluid dynamics under a condition of extremely high impulsive stress; the magnitude of an initially formed shock wave is taken to be of the order of 100 MPa in the present study. The present treatment of the boundary is valid when the high pressure beyond the elastic limit is applied to the material. The plastic deformation of the tissue material mentioned in the experimental paper (e.g. Eisenmenger 2001) is an important factor for the mechanics of the tissue material. This treatment will be discussed in future works. Using (2), we can obtain the sound speed in a material as

$$a = \sqrt{\frac{\gamma\left(p+\Pi\right)}{\rho}}\,, \tag{3}$$

where the values of γ and Π for air, water, gelatin, liver, stone, and fat are listed in table 1. The acoustic impedance for each material is expressed as ρa. The values of γ and Π are determined so that the density and acoustic impedance agree with their physical properties (Takahira *et al* 2008, 2009). The values of density and acoustic impedance listed in table 1 for gelatin, liver, stone, and fat are evaluated from Goss *et al* (1978), Ophir and Jaeger (1982) Kodama and Takayama (1998), and Heimbach *et al* (2000). The acoustic impedance of gelatin is similar to that of liver, kidney, human arteries, blood, and other organs (Goss *et al* 1978, Ophir and Jaeger 1982).

2.2. Interface capturing

Two kinds of interfaces were considered; air-water and water-tissue interfaces (see figure 1). An interface is discriminated by the level set function, φ, which is a signed distance function from the interface (Sussman *et al.* 1994). For $\varphi < 0$, the region is defined as water, for $\varphi > 0$, the region as air and tissue. The interface is defined by the set of $\varphi = 0$. Thus two kinds of fluids are distinguished by the sign of the level set function. Using the level set function, the unit normal $\boldsymbol{n}$ at each grid point is defined as

$$\boldsymbol{n} = \frac{\nabla\varphi}{|\nabla\varphi|}. \tag{4}$$

The level set function φ obeys the following equation:

$$\frac{\partial\varphi}{\partial t} + u\frac{\partial\varphi}{\partial r} + v\frac{\partial\varphi}{\partial z} = 0. \tag{5}$$

In the GFM, the normal direction is determined using the level set function. Thus, the reinitialization procedure is necessary to maintain φ as a true distance function because the level set function φ is diffused or distorted by the flow field. The reinitialization equation is given as

$$\frac{\partial\varphi}{\partial t^*} + S(\varphi_0)(1 - |\nabla\varphi|) = 0, \tag{6}$$

where t^* is fictitious time and $S(\varphi_0)$ is the sign function in which φ_0 is the initial value of φ for solving the equation (Sussman *et al.* 1994). However, this procedure sometimes slightly changes the location of the interface and smoothes the interface. In order to avoid the numerical diffusion, we apply a high order discretization scheme with the 5th–order weighted ENO (WENO) scheme (Jiang and Peng 2000) and the hybrid particle level set method (Engright *et al* 2002). In the hybrid particle level set method, massless marker particles are used to enhance the resolution of the interface. In this method, the massless signed marker particles are passively advected along by using the flow. The particles are advected with the fluid velocity and the level set function is corrected with these particles. The mass conservation of the hybrid particle level set method is better because it has a sub–grid resolution. Takahira *et al* (2008, 2009) showed that it works well in conserving the mass of the bubbles for the shock-bubble interactions. We use the 3rd–order TVD–Runge Kutta scheme to update (5) and (6).

2.3. Ghost fluid method

The ghost fluid method (GFM) is applied to solve (1) and (2) for three types of fluids with different physical properties: air, water, and tissue (gelatin, liver, stone, and fat) (see figure 1). The ghost fluids are defined at every grid point in the computational domain so that each grid point contains the mass, momentum, and energy of the real fluid that exists at that grid point, and a ghost mass, momentum and energy of the other fluid that does not really exist at that grid point (Fedkiw *et al* 1999, Osher and Fedkiw 2003). For example, fluid 1 exists in the region where $\varphi > 0$, and fluid 2 exists in the region where $\varphi < 0$. Then, the artificial fluid for fluid 1 (ghost fluid 1) is defined in the region where $\varphi < 0$, and the artificial fluid for fluid 2 (ghost fluid 2) is also defined in the region where $\varphi > 0$. Once the ghost fluids are defined, we can use the standard method used for a single-phase fluid to update the Euler equations. After updating the Euler equations for each fluid separately, the updated level set function is used to decide which of the two fluids is valid at each grid point. The valid fluid is kept and the other one is discarded so that only one fluid is defined at each grid point.

Usually in the GFM, since the pressure and normal velocity are continuous across the interface, the pressure and normal velocity of the ghost fluid are copied over from the real fluid in a node by node fashion. On the other hand, since the entropy and tangential velocity are discontinuous across the interface, they are defined using constant extrapolation in the normal direction. However, when one fluid is very stiff, the determination of the values of the ghost fluid should be changed to avoid numerical oscillation. One problem in applying the original GFM to the interfacial motion in which the one fluid is stiff (e.g. gas-liquid interface) is the unrealistic pressure oscillations near the interface, which sometimes leads to the divergence of the solution. For stiff fluids, therefore, to avoid the divergence, careful treatment is needed for the variables on both sides of the interface. To do this, in IGFM (improved ghost fluid method) (Takahira *et al* 2008, 2009), the Riemann solutions (Toro 1997) are utilized for correcting the values at the boundary nodes in the Eulerian mesh. For details of the Riemann correction, the reader is referred to Takahira *et al* (2009). Also, in IGFM, the definition of ghost values across the gas-liquid interface is modified as follows. For the ghost fluid of air, the pressure is extrapolated from real air in addition to entropy and tangential velocity. For the ghost fluid of liquid, the normal velocity as well as entropy and tangential velocity is extrapolated from real liquid (Osher and Fedkiw 2003). For the water-tissue boundary, we apply the original GFM extrapolation procedure.

We use the fast extension method based on the fast marching method for the extrapolation (Adalsteinsson and Sethian 1999).

2.4. Numerical model

The computational domain and bubble arrangement are shown in figure 1. An air bubble with radius R_0 (= 0.8 mm) is initially at rest near the boundary. An incident shock wave propagates from the left-hand side (upstream side) of the bubble. Height H in the r direction is taken to be $4R_0$, length L_s behind the shock wave is taken to be $30.6R_0$, distance L_{sb} between the bubble centroid and the shock front is taken to be $1.4R_0$, and thickness L_t of the wall is taken to be 6.8 R_0. The wave form has a long tail as shown in figure 2. The length of the liquid domain behind the shock wave, L_s is chosen so that the almost entire profile of the shock wave with sufficient length of tail contains in the computational domain. L_{sb} is an entrance length of the shock wave and is not a crucial value for the simulation. The H is chosen to reduce the artificial reflection of the pressure wave at the end of the computational domain during the present computational period. The influence of the thickness of L_t is discussed in a later section; we have confirmed that the present width of L_t is sufficient. In addition, L_0 is the initial distance between the bubble centroid and the boundary. Symmetric boundary conditions are used at the z-axis. In the present simulations, zero gradients of pressure and velocities are applied at the top, left, and right boundaries. Although this is not the perfect non-reflection condition, the artificial reflection of the pressure wave at the end of the computational domain has negligible effects on the bubble motion if the computational region is sufficiently large during the period of interest. The location of the interface is defined as a set of points satisfying $\varphi = 0$. To simulate bubble collapse near the boundary, as shown in figure 1, three types of materials, i.e., air inside the bubble, water, and tissue, should be distinguished. We define $\varphi < 0$ as the region occupied by water; the physical quantities for water are utilized in the region $\varphi < 0$. The region $\varphi > 0$ is for air or tissue. To distinguish between air and tissue regions that have the same positive sign of the level set function, the tissue region is determined by considering the deformation of the tissue boundary using the tissue position $z = z_t$ shown in figure 1 (Takahira *et al* 2008, 2009).

The influence of grid size has been discussed in the third author's work (Takahira *et al* 2009). They showed that the grid $\Delta r/R_0 = \Delta z/R_0 = 0.02$ is sufficient to capture the bubble behaviors and its collapse time. Hence, we adopt the grid size 0.02 for the simulations. The time increment is $\Delta t = 1.33 \times 10^{-9}$ s in the present study.

2.5. Incident shock wave

The pressure profile of the incident shock wave is determined from the experimental data of Kodama and Takayama (1998), as shown in figure 2:

$$p(z) = a\exp[b(z - L_s)] + p_0, \qquad z \le L_s, \tag{7}$$

where a and b are constants (a = 108 MPa, b = 393.9), p_0 = 1.013 × 10^5 Pa (the initial pressure in front of the incident shock wave), L_s = 2.448 × 10^{-2} m, and the shock Mach number is 1.054. The maximum pressure of the incident shock wave p_s (= a + p_0) is taken to be ten times larger than that of Kodama and Takayama (1998). One reason for this choice is that the local maximum pressure of the shock wave in the actual ESWL is approximately 100 MPa (Coleman and Saunders 1993, Loske 2010), which is the same order of the present simulation. Another reason is attributed to the practical numerical issue. As can been seen in the later section, the lifetime of the bubble increases with a decrease in the shock wave intensity. The longer lifetime needs a wider computational domain to avoid false reflection of the pressure waves from the outer edge of the domain; the bubble gets distorted when a weak shock interacts with it. Bubble collapse when interacting with weak shock waves will be discussed in a future work using a multigrid method with a wider computational domain.

3. Results and discussion

3.1. Collapse motions of bubble, liquid jet formation, and shock wave radiation

Figure 3 shows the collapse motions of a bubble near the gelatin boundary in water under the condition of R_0 = 0.8 mm and L_0/R_0 = 1.2. The length of the bubble radius and the material of the boundary are selected in reference to the previous experiment (Kodama and Takayama 1998).

Figure 3(a) depicts bubble shapes and schlieren images, whereas figure 3(b) depicts the bubble shapes and pressure contours. Figure 3(c) depicts enlarged figures from the 10th to 15th frames presented in figure 3(b). As shown in the 3rd frame of figures 3(a) and 3(b), a strong expansion wave is produced in water after an incident shock wave is reflected at the bubble surface, because the acoustic impedance of water is much larger than that of air in the bubble (see table 1). The pressure gradient formed around the bubble after the incident shock wave passes through the bubble leads to the bubble collapse. Since the pressure gradient at the upstream side is steeper than that at the downstream side, the bubble wall velocity is faster at the upstream side (see figure 7 which is placed later). The downstream side of the bubble goes upstream with lower velocity. As a result, when the bubble starts to collapse, a sink flow occurs around the bubble. Then, the incident shock wave impacts the gelatin surface (the 4th frame of figures 3(a) and 3(b)). Although the impact of the shock wave on the gelatin surface causes a displacement towards the downstream direction, this displacement is very small at this stage. The shock wave transmits into the gelatin wall without reflection because the acoustic impedance of water is almost equal to that of gelatin (the 5th frame of figures 3(a) and 3(b)). As the bubble collapses, the gelatin boundary deforms so as to be attracted towards the bubble (10th frame of figure 3(c)). This is due to the sink flow formed around the collapsing bubble: the deformation of the gelatin boundary is induced by the bubble collapse. We can also observe a small deformation on the upper bubble surface in the 10th frame; the upper surface impacts the bottom one in the 11th frame. When this impact occurs, a strong shock wave is generated at the impact point. The shock wave hits the gelatin boundary (12th frame) and propagates inside the gelatin. The impact of the strong shock wave causes the deformation of the gelatin boundary in a concave shape (13th, 14th, and 15th frames of figure 3(c)).

The experiment by Kodama and Takayama (1998) showed that the collapse time of the bubble with the initial radius of 0.8 mm induced by the shock wave was approximately 11 μs (the maximum pressure of the incident shock was 10.2 ± 0.5 MPa). The collapse time in the simulation is approximately one-third smaller than that of the experiment (approximately 3.8 μs for the present simulation). This discrepancy is caused by the difference in the maximum pressure of the incident shock wave between the experiment and the present simulation (p_s = 108 MPa). The collapse time of an empty spherical cavity, the Rayleigh collapse time t_c^R, is evaluated as $t_c^R = 0.915 R_0 / \sqrt{\Delta p / \rho_s}$ (Rayleigh 1917), where $\Delta p = p_s - p_0$, and ρ_s is the density behind the incident shock wave in the present study. Because the collapse time is inversely proportional to $\sqrt{\Delta p}$, the simulation result becomes approximately one-third smaller. Except for the collapse time, there is an overall qualitative agreement for the bubble behavior between the experiment and the simulation.

3.2. Influence of tissue properties on bubble collapse

Here, we investigate the influence of tissue properties on bubble collapse. Figures 4(a), 4(b), and 4(c) show the pressure contours and bubble shapes near a stone, fat, or liver boundary in the case of L_0/R_0 = 1.2, respectively. The bubble collapse near a stone is somewhat different from that near gelatin. When the bubble collapses near the stone boundary, the large acoustic impedance of the stone (see table 1), which is almost three times larger than that of gelatin, contributes to the generation of a stronger shock wave by the bubble collapse. As is evident in figure 4(a) (ii), when an incident shock wave hits the stone, the compression wave reflects at the stone boundary. The maximum pressure of the compression wave is approximately 54% of the incident shock wave (Leighton 1994). The compression wave increases the ambient water pressure around the bubble. As a result, the bubble collapses in a higher pressure field near the stone boundary than that near the gelatin boundary, which induces the acceleration of the formation of liquid jet with the bubble collapse (figure 4(a) (iii)). The acceleration of the jet leads to the higher impulsive pressure at the point of the jet impact (figure 4(a) (iv)). On the other hand, the acoustic impedance of fat is 16% smaller than that of water (see table 1).

Thereby, when the incident shock wave hits the fat boundary, the expansion wave is reflected (the expansion wave is not shown clearly in figure 4(b) (ii) because of the weak reflection of the incident shock wave at the boundary). The minimum negative pressure of the expansion wave is approximately 9% of the incident shock wave (Leighton 1994). Hence, the bubble collapses in a lower pressure field near the fat boundary than that near the gelatin one. As a result, the collapse time becomes slightly longer. Figure 4(c) shows the results obtained in the case of the liver boundary. Because the acoustic impedance of the liver is almost the same as that of gelatin (see table 1), the incident shock wave propagates to the boundary without the reflection wave; similar behaviors of the bubble and boundary are observed for the case of gelatin.

Figure 5 shows the relationship between the bubble collapse time t_c and the initial distance between the bubble centroid and the boundary L_0/R_0 for each material, where the minimum volume of bubble determines the collapse time t_c. The orange square denotes gelatin, the green circle denotes the liver, the red triangle denotes the stone, and the blue cross denotes fat. The time is nondimensionalized by $t_0 = R_0 / \sqrt{\Delta p / \rho_s}$ =2.48 μs. For gelatin and liver, the bubble collapse time does not depend on L_0/R_0. On the other hand, for the stone or fat boundary, the bubble collapse time decreases or increases with a decrease in L_0/R_0, respectively. These results are attributed to the reflection of the incident shock wave formed at the boundary (shown in figures 4(a) and 4(b)). Bubble collapse is induced by the pressure difference between the air inside a bubble and the ambient liquid. As the distance L_0/R_0 decreases, the exposure time of the higher or lower pressure field formed by the reflection wave increases. As a result, bubble collapse is accelerated or decelerated by the pressure difference; the bubble collapse time decreases or increases near stone or fat.

Typically, the bubble collapse time under the constant pressure field of ambient liquid decreases as the mass of the compliant boundary decreases (Duncan and Zhang 1991, Shima *et* *al* 1989). Although the density of fat takes approximately 92% and that of stone takes 155% for gelatin, the present simulation results take the opposite tendency to the aforementioned results; the reflection waves at the tissue boundaries are dominant for bubble collapse in the present situation.

Figures 6(a) and 6(b) respectively show time histories of equivalent bubble radii and translational displacements of bubble centroids for gelatin (orange line), liver (green line), stone (red line), and fat boundaries (blue line); $L_0/R_0 = 1.2$. The equivalent bubble radius is defined by $R(t) = (3V/4\pi)^{1/3}$, where V is the bubble volume. The translational displacement is determined as $\delta z = z_b(t) - z_b(t = 0)$, where $z_b = \int_V z \, dV/V$. The radius history and translational displacement for stone are different in four cases: the bubble radius becomes smaller, and the displacement of the bubble centroid near the stone boundary is reduced before bubble collapse (the collapse time is approximately $t/t_0 = 1.4$). The suppression of the displacement is also caused by the reflection of the incident shock wave at the stone boundary, which induces the translational motion of a bubble away from the boundary. However, after bubble collapse, the translational motion toward the stone boundary is accelerated owing to the faster liquid jet at the upstream surface of the bubble (shown in figure 7(c)). For fat, because of the low pressure field of ambient liquid formed by the expansion wave, the minimum radius becomes slightly larger and the collapse time increases.

The formation of liquid jet at the bubble surface is the prominent feature for the nonspherical bubble collapse. To investigate the velocity of the liquid jet, the velocities at the north and south poles of the bubble surface in the case of $L_0/R_0 = 1.2$ are shown in figure 7. The north pole is the upstream bubble surface (opposite side of the tissue boundary) on the z axis, and the south pole is the downstream surface. Figures 7(a)–7(d) are the results when the bubble collapses near the gelatin, liver, stone, or fat boundary, respectively. The velocity on the positive z direction is indicated by the positive sign. The velocity is nondimensionalized by $\sqrt{\Delta p/\rho_s}$=322.75 m/s. For figure 7(a) (gelatin), when the incident shock wave hits the north pole, the velocity at the north pole, v_N, increases stepwise. Because the bubble volume decreases, the velocity at the south pole, v_S, becomes negative in the z direction. v_N is faster than v_S, which causes the formation of liquid jet toward the gelatin boundary. After the jet impacts, both surfaces attach to each other and the velocities at both sides of the thin gas layer decrease suddenly, v_N is almost the same as v_S. The velocities near gelatin and liver have the same tendency because of the similar acoustic impedance of the boundary (see figure 7(a) and 7(b)). When the bubble collapses near the stone boundary (figure 7(c)), the maximum velocity at the north pole becomes 1.7 times larger than that near the gelatin (liver) boundary. For the fat boundary, the maximum velocity of the north poles becomes 8% smaller than that of gelatin (liver). The reasons for the above results are the reflection of the incident shock wave at the boundary shown in figure 4.

When the liquid jet impacts, the magnitude of the impulsive pressure (water hammer pressure p_{wh}) generated at the impact point obeys the following equation (Leighton 1994, Johnsen and Colonius 2009):

$$p_{\mathrm{wh}} = \frac{1}{2}\rho_{\mathrm{w}} a_{\mathrm{w}} v_{\max}^{\mathrm{rel}}, \tag{8}$$

where ρ_w and a_w are the density and sound speed of water, respectively, and $v_{\max}^{\mathrm{rel}}$ is defined as $v_{\max}^{\mathrm{rel}} = \max(v_N - v_S)$. For the results of gelatin, liver, stone, and fat as shown in figure 7, the evaluated values using (8) are $p_{wh}/\Delta p$ = 9.03, 9.34, 18.17, and 8.40, respectively. The impulsive pressure leads to the generation of a strong shock wave from the collapsing bubble.

The time histories of pressure at the gelatin, liver, stone, and fat boundaries on the z axis are shown in figure 8(a) ($L_0/R_0 = 1.2$). The pressure at the boundaries increases impulsively because of the impact of the shock waves generated by bubble collapse. Because bubble collapse is accelerated by the reflection of an incident shock wave at the stone boundary, the impulsive maximum pressure at the stone boundary is almost twice that at the gelatin (liver) boundary. Figure 8(b) shows the time histories of displacement of the boundary. The displacement is defined as $\eta = z_t(t) - z_t(t = 0)$, where z_t is the location of the boundary on the z axis. The negative sign of η indicates that the boundary moves toward the bubble. As the bubble collapses, the boundary is attracted to the bubble because of the sink flow induced by the bubble. Then, the boundary moves downstream because of the influence of impulsive pressure of the shock waves generated by the bubble collapse. Although the higher impulsive pressure is imposed on the stone boundary, the displacement of the stone boundary is smaller than that of the gelatin (liver) boundary because stone is heavier than gelatin (liver). In contrast, the fat boundary is most attracted to the bubble because of the lighter density.

The influence of the initial bubble radius on the shock–bubble interaction is discussed briefly. Figures 9(a) and 9(b) show the time histories of the average pressure of air inside the bubble, p_g, and the pressure at the gelatin boundary for the initial bubble radii $R_0 = 0.4$ mm, 0.8 mm, 1.2 mm, and 1.6 mm. The same profile of the incident shock wave in figure 2 is used for the bubbles of different sizes. Since the pressure profile is the same with each other, the high–pressure region of the incident shock wave becomes relatively smaller as the initial radius becomes larger in comparison with bubble size. The dotted line is the case of $R_0 = 0.4$ mm, the thin solid line is that of $R_0 = 0.8$ mm, the thick solid line is that of $R_0 = 1.2$ mm, and the thin broken line is that of $R_0 = 1.6$ mm. For each case, the initial bubble–boundary distance is $L_0/R_0 = 1.2$. From figure 9(a), the smaller the initial bubble size becomes, the higher the average pressure inside the bubble becomes and the shorter the collapse time becomes. This is because when the initial bubble radius is small, the exposure time of the high–pressure field that occurs due to the incident shock wave is relatively long, which leads to more violent collapse. These results qualitatively agree with the experiments performed by Kodama and Takayama (1998). The violent bubble collapse induces a stronger shock wave generation from the bubble. Thus, as shown in figure 9(b), the pressure at the gelatin boundary becomes higher as the initial bubble radius becomes smaller.

Also, the influence of the thickness of the tissue material is discussed. Figures 10(a) and 10(b) show the time histories of the bubble radius and the displacement of the stone boundary for L_t/R_0 = 3.4, 6.8, and 13.6. As evident from figures 10(a) and 10(b), the negligible effect is found in the thickness of the tissue material. Thus, the reflection on the right edge of the material is sufficiently small when L_t/R_0 = 6.8 is used in the present computation.

Hereafter, the influences of bubble collapse position on the maximum liquid jet velocity and the maximum pressure at tissue boundary are discussed. Figure 11 shows the relationship between the bubble collapse position L_c/R_0, where L_c is defined by the length between the tissue boundary and the downstream surface of the bubble on the z axis when the liquid jet impacts. The red triangle denotes the stone, the green circle denotes the liver, the orange square denotes gelatin, and the blue cross denotes fat. L_c/R_0 is in proportion to L_0/R_0 for each tissue. In the case of stone, L_c/R_0 becomes slightly longer than that of the other tissues because of the suppression of the translational motion of the bubble due to the reflection of compression wave, as shown in figure 6(b).

Figure 12(a) shows the relationship between the maximum jet velocity $v_{\max}^{\mathrm{rel}}$ and L_c/R_0. As evident in the figure, the maximum jet velocity near the stone boundary increases with a decrease in L_c/R_0. This is because, as shown in the figure 5, the reflection of the compression wave at the boundary enhances the bubble collapse more strongly when the bubble–tissue distance becomes shorter. In contrast, for the fat boundary, the maximum jet velocity decreases with a decrease in L_c/R_0 because of the reflection of the expansion wave. As mentioned above, the increase in the maximum jet velocity induces the generation of strong shock wave from the collapsing bubble.

Figure 12(b) shows the relationships between the maximum pressures p_{max} at gelatin, liver, stone, and fat boundaries on z axis and L_c/R_0. When the shock wave caused by the bubble collapse hits the boundary, the pressure at the boundary takes the maximum value. As shown in the figure, the maximum pressure decreases with an increase in L_c/R_0. The solid lines ($p_{max}/\Delta p = A/z + B$) for each tissue are shown in the figure. The constant values A and B are determined using the least-squares method (for gelatin, A = 2.460, B = 0.006; liver, A = 2.606, B = -0.033; stone, A = 5.855, B = 0.570; fat, A = 1.952, B = 0.119). The maximum pressure decreases in inverse proportion to L_c/R_0, which agrees with the results by Johnsen and Colonius (2008).

3.3. Impulse at tissue boundary

The following factors are responsible for tissue damage in shock-wave lithotripsy: the shear force induced by focused shock waves or bubble collapse/expansion (Lokhandwalla *et al* 2001a, b), penetration of liquid jet with the collapsing bubble (e.g. Kodama and Takayam 1998, Freund *et al* 2009, Ohl *et al* 2009), and impulsive pressure of shock wave resulting from bubble collapse. Here, we focus on the impulsive pressure of the shock wave resulting from bubble collapse and we conduct a quantitative evaluation of the mechanical effect of the tissue damage using *impulse*. The impulse of a shock wave has also been used to evaluate the fluorophore uptake into the living cells (Kodama *et al* 2000) and the penetration of water molecule into the hydrophobic region of the bilayer (Koshiyama *et al* 2006).

Figure 13(a) shows the evaluation method of impulses I_s and I_c on the z axis at the tissue boundary using the pressure profiles $p(t)$ (in case L_0/R_0 is equal to 1.2, the pressure profile is shown in figure 8(a)), where I_s is the impulse caused by the impact of the incident shock wave and I_c is that by the impact of the shock wave generated from bubble collapse. The impulses I_s and I_c are defined as follows:

$$I_{\mathrm{s}} = \int_{t_1}^{t_2} p(t)\mathrm{d}t, \quad I_{\mathrm{c}} = \int_{t_2}^{t_3} p(t)\mathrm{d}t, \tag{9}$$

where the definitions of t_1, t_2 and t_3 are shown in figure 13(a). The increasing and decreasing thresholds to evaluate the impulse I_c are defined empirically to estimate only the value of the impulse of the shock wave by the bubble collapse. The gray and hatched areas in the figure are used to evaluate the impulses, where τ_s (= $t_2 - t_1$) is the duration time of I_s and τ_c (= $t_3 - t_2$)is that of I_c. I_{total} is the total impulse defined by $I_{total} = I_s + I_c$. The duration times τ_s and τ_c for each tissue are shown in figures 13(b) and 13(c), respectively. In all cases, τ_s is longer than τ_c for each tissue and becomes shorter with a decrease in L_c/R_0. The decrease in τ_s for stone is particularly pronounced in all tissues; violent bubble collapse occurs when the bubble–tissue distance becomes shorter, and the collapse time decreases. As a result, the duration time τ_s becomes shorter. In contrast, for duration time τ_c, as L_c/R_0 decreases, the rate of decay of the spherical shock wave by the bubble collapse decreases in all tissues. Hence, the shock intensity at the boundary increases and τ_c becomes long.

The dimensionless I_{total}/I_{ref} is plotted with respect to L_c/R_0 in figure 14(a), where I_{ref} is the impulses of the impact by the incident shock wave without a bubble in the cases of gelatin, liver, stone, and fat boundaries, respectively (for gelatin, $I_{ref}/(\Delta p \cdot t_0) = 0.48$; liver, $I_{ref}/(\Delta p \cdot t_0) = 0.49$; stone, $I_{ref}/(\Delta p \cdot t_0) = 0.74$; fat, $I_{ref}/(\Delta p \cdot t_0) = 0.43$). The increasing and decreasing thresholds to evaluate I_{ref} are $p/\Delta p$ = 0.05. The duration time of I_{ref} for gelatin is τ_{ref}/t_0 = 1.57, for liver τ_{ref}/t_0 = 1.58, for stone τ_{ref}/t_0 = 1.77, and for fat τ_{ref}/t_0 = 1.52. I_{ref} and τ_{ref} of stone take a higher value because of the reflection of the compression wave at the boundary, as previously stated. The impulse I_{total}/I_{ref} of each tissue material is inversely proportion to L_c/R_0 and is close to the dimensionless value of I_{ref} (shown as a dashed line in the figure) asymptotically with increasing L_c/R_0. I_{total}/I_{ref} has a similar tendency for each tissue material. The fraction of impulse by the bubble collapse I_c for the value of I_{total} is shown in figure 14(b). The fraction decreases with an increase in L_c/R_0. The impulse I_c is more than 50% of I_{total} when L_c/R_0 is less than 0.9; most of the higher total impulse I_{total} shown in figure 14(a) is composed of the impulse I_c.

To analyze the influence of impulse I_c on tissue damage, we investigate the relationship between the tissue boundary deformation and impulse I_c. Figure 15(a) shows the displacement of the tissue boundary toward the positive direction on the z axis during τ_c, $\delta\eta/R_0$, versus I_c/I_{ref} for each tissue, where $\delta\eta$ is defined by $\delta\eta = \eta(t_3) - \eta(t_2) = z_t(t_3) - z_t(t_2)$. It is found that $\delta\eta/R_0$ increases with an increase in I_c/I_{ref} in a curved line. By using the results of figures 13(c) and 15(a), the tissue boundary velocity v_t, i.e., the averaged rate of the tissue deformation during τ_c can be estimated. The relationship between the tissue boundary velocity $v_t / \sqrt{\Delta p / \rho_s}$ and impulse I_c/I_{ref} is shown in figure 15(b), where v_t is defined by $v_t = \delta\eta/\tau_c$. As shown in the figure, the tissue boundary velocity $v_t / \sqrt{\Delta p / \rho_s}$ increases in proportion to I_c/I_{ref} for each tissue. These results suggest that impulse I_c has a significant correlation with the displacement of the tissue boundary. This tissue displacement caused by bubble collapse leads to incipient stone fragmentation and pitting damage of tissue. The results of the present study reveal that the impulse by the bubble collapse is the key factor in the deformation of the tissue boundary and that IGFM is a useful method to analyze the shock wave–bubble interaction near the various tissues with different acoustic impedances.

4. Conclusion

In the present study, numerical simulations were conducted to examine the interaction of an incident shock wave with a bubble near a soft or rigid tissue using the improved ghost fluid method. Three kinds of materials (air, water, and tissue) were used as the fluids. We focused on bubble deformation and collapse near each tissue. For the stone boundary, violent bubble collapse occurs because of the compression wave generated by the reflection of the incident shock wave. The collapse becomes weak near the fat boundary because of the expansion wave generated by the reflection of the incident shock. Bubble deformation and collapse depend not only on the reflection waves but also on the bubble–tissue distance. The impulse obtained from the temporal evolution of pressure at the tissue boundary was used to evaluate the boundary deformation. From the pressure profile, two types of impulses were obtained. One is a result of the impact of the incident shock wave and the other is a result of the impact of the shock wave by the bubble collapse. It is found that the impulse by the bubble collapse has a significant correlation with the displacement of the tissue boundary, which leads to incipient tissue damages or stone fragmentation. In future, we could obtain a more precise description of the shock wave–bubble interaction near the tissue boundary by incorporating the elastic–plastic deformations of the tissue material into the improved ghost fluid method.

References

Adalsteinsson D and Sethian J A 1999 The fast construction of extension velocities in level set method *J. Comput. Phys.* **148** 2-22

Calvisi M L, Iloreta J I and Szeri A J 2008 Dynamics of bubbles near a rigid surface subjected to a lithotripter shock wave. Part 2. Reflected shock intensities non-spherical cavitation collapse *J. Fluid. Mech.* **616** 63-97

Coleman A J and Saunders J E 1993 A review of the physical properties and biological effects of the high amplitude acoustic field used in extracorporeal lithotripsy *Ultrasonics* **31** 75-89

Duncan J H and Zhang S 1991 On the interaction of a collapsing cavity and a compliant wall *J. Fluid. Mech.* **226** 401-23

Eisenmenger W 2001 The mechanisms of stone fragmentation in ESWL *Ultrasound Med. Biol.* **27** 683-93

Enright D, Fedkiw R, Ferziger J and Mitchell I 2002 A hybrid particle level set method for improved interface capturing *J. Comput. Phys.* **183** 83-116

Fedkiw R P, Aslam T, Merriman B and Osher S 1999 A non-oscillatory Eulerian approach to interfaces in multimaterial flows (the ghost fluid method) *J. Comput. Phys.* **152** 457-92

Fedkiw R P 2002 Coupling an Eulerian fluid calculation to a Lagrangian solid calculation with the ghost fluid method *J. Comput. Phys.* **175** 200-24

Freund J B, Shukla R K and Evan A P 2009 Shock-induced bubble jetting into a viscous fluid with application to tissue injury in shock-wave lithotripsy *J. Acoust. Soc. Am.* **126** 2746-56

Goss S A, Johnston R L and Dunn F 1978 Comprehensive compilation of empirical ultrasonic properties of mammalian tissues *J. Acoust. Soc. Am.* **64** 423-57

Heimbach D, Jacobs D, Müller S C and Hesse A 2000 Influence of alkaline solutions on chemolitholysis and lithotripsy of uric acid stones *Eur. Urol.* **38** 621-6

Jiang G -S and Peng D 2000 Weighted ENO schemes for Hamilton-Jacobi equations *SIAM J. Sci. Comput.* **21** 2126-43

Johnsen E and Colonius T 2006 Implementation of WENO schemes in compressible multicomponent flow problems *J. Comput. Phys.* **219** 715-32

Johnsen E and Colonius T 2008 Shock-induced collapse of a gas bubble in shockwave lithotripsy *J. Acoust. Soc. Am.* **124** 2011-20

Johnsen E and Colonius T 2009 Numerical simulations of non-spherical bubble collapse *J. Fluid. Mech.* **629** 231-62

Kodama T and Takayama K 1998 Dynamic behavior of bubbles during extracorporeal shock-wave lithotripsy *Ultrasound Med. Biol.* **24** 723-38

Kodama T, Hamblin M R and Doukas A G 2000 Cytoplasmic molecular delivery with shock waves: importance of impulse *Biophys. J.* **79** 1821-32

Koshiyama K, Kodama T, Yano T and Fujikawa S 2006 Structual change in lipid bilayers and water penetration induced by shock waves: molecular dynamics simulations *Biophys. J.* **91** 2198-205

Leighton T G 1994 *The Acoustic Bubble* (London: Academic Press)

Lingeman J E, McAteer J A, Gnessin E and Evan A P 2009 Shock wave lithotripsy: advances in technology and technique *Nat. Rev. Urol.* **6** 660-70

Lokhandwalla M and Sturtevant B 2001a Mechanical haemolysis in shock wave lithotripsy (SWL): I. Analysis of cell deformation due to SWL flow-fields *Phys. Med. Biol.* **46** 413-37

Lokhandwalla M, McAteer J A, Williams Jr J C and Sturtevant B 2001b Mechanical haemolysis in shock wave lithotripsy (SWL): II. In vitro cell lysis due to shear *Phys. Med. Biol.* **46** 1245-64

Loske A M 2010 The role of energy density and acoustic cavitation in shock wave lithotripsy

Ultrasonics **50** 300-5

Ohl S W, Klaseboer E and Khoo B C 2009 The dynamics of a non-equilibrium bubble near bio-materials *Phys. Med. Biol.*, **54** 6313-36

Ophir J and Jaeger P 1982 A ternary solution for independent acoustic impedance and speed of sound matching to biological tissues *Ultrasonic Imaging* **4** 163-70

Osher S and Fedkiw R P 2003 *Level set methods and dynamic implicit surface* (New York:Springer-Verlag)

Rayleigh L 1917 On the pressure developed in a liquid during the collapse of a spherical cavity *Phil. Mag.* **34** 94-8

Saurel R and Abgrall R 1999 A simple method for compressible multifluid flows *SIAM J. Sci. Comput.* **21** 1115-45

Semins M J, Trock B J and Matlaga B R 2008 The effect of shock wave rate on the outcome of shock wave lithotripsy: a meta-analysis *J. Urol.* **179** 194-7

Shima A, Tomita Y, Gibson D C and Blake J R 1989 The growth and collapse of cavitaion bubbles near composite surfaces *J. Fluid. Mech.* **203** 199-214

Shu C -W and Osher S 1989 Efficient implementation of essentially non-oscillatory shock-capturing schemes II *J. Comput. Phys.* **83** 32-78

Sussman M, Smereka P and Osher S 1994 A level set approach for computing solutions to incompressible two-phase flow *J. Comput. Phys.* **114** 146-59

Takahira H, Matsuno T and Shuto K 2008 Numerical investigations of shock-bubble interactions in mercury *Fluid Dyn. Res.* **40** 510-20

Takahira H, Kobayashi K and Matsuno T 2009 Direct numerical simulations of interaction of strong shock waves with nonspherical gas bubbles near glass boundaries in mercury *Int. J. Emerging Multidisciplinary Fluid Sci.* **1** 85-99

Tham L M, Lee H P and Lu C 2007 Enhanced kidney stone fragmentation by short delay tandem conventional and modified lithotriptor shock waves: a numerical analysis *J. Urol.* **178** 314-9

Toro E F 1997 *Riemann solvers and numerical methods for fluid dynamics* (Berlin:Springer-Verlag)

Yilmaz E, Batislam E, Basar M, Tuglu D, Mert C and Basar H 2005 Optimal frequency in extracorporeal shock wave lithotripsy: prospective randomized study *Urology* **66** 1160-4

Zukas J A, Nicholas T, Swift H F, Greszczuk L B and Curran D R 1982 *Impact Dynamics* (New York: John Wiley & Sons)

Captions

Table 1. Parameters for each material.

Figure 1. Schematic of present simulation.

Figure 2. Incident shock wave profiles. The profile was obtained from the experimental data in Kodama and Takayama (1998).

Figure 3. Bubble collapse near gelatin at L_0/R_0 = 1.2: (a) schlieren images; (b) pressure contours; (c) enlarged figures for (b).

Figure 4. Bubble collapse near stone, fat, and liver boundaries at L_0/R_0 = 1.2: (a) near stone; (b) near fat; (c) near liver.

Figure 5. Bubble collapse time versus L_0/R_0.

Figure 6. Bubble radius and translational motion of bubble at L_0/R_0 = 1.2: (a) bubble radii; (b) trajectories of the bubble centroid.

Figure 7. Liquid jet velocities of bubble near each tissue material at L_0/R_0 = 1.2.

Figure 8. Time histories of pressure at tissue boundary and its deformation at L_0/R_0 = 1.2: (a) pressure at the boundary; (b) displacement of the boundary.

Figure 9. Time histories of average pressure inside bubble and pressure at gelatin boundary for L_0/R_0 = 1.2: (a) average pressure of air inside bubble; (b) pressure at gelatin boundary.

Figure 10. Time histories of bubble radius and displacement of stone boundary for L_t/R_0 = 3.4, 6.8, and 13.6: (a) bubble radius; (b) displacement of stone boundary.

Figure 11. Bubble collapse position for L_0/R_0.

Figure 12. Maximum liquid jet velocity and the maximum pressure at tissue boundary: (a) maximum jet velocity versus L_c/R_0; (b) maximum pressure at tissue boundary versus L_c/R_0.

Figure 13. Definition of impulse and duration time of impulse: (a) schematic of evaluation method of impulse; (b) duration times τ_s versus L_c/R_0; (c) duration times τ_c versus L_c/R_0.

Figure 14. Impulse at each tissue boundary: (a) total impulse for each tissue versus L_c/R_0; (b) fraction of impulse caused by bubble collapse I_c/I_{total} versus L_c/R_0.

Figure 15. Displacement of tissue boundary and tissue boundary velocity as a result of bubble collapse: (a) displacement of tissue boundary versus I_c/I_{ref}; (b) tissue boundary velocity versus I_c/I_{ref}.

Table 1. Parameters for each material.

	γ	Π (Pa)	Density (kg m^{-3})	Acoustic impedance (kg s^{-1} m^{-2})
Air	1.40	0	1.2	4.10×10^{2}
Water	4.40	6.00×10^{8}	998.6	1.62×10^{6}
Gelatin	4.04	6.10×10^{8}	1061.0	1.62×10^{6}
Liver	4.18	6.20×10^{8}	1075.0	1.67×10^{6}
Stone	1.66	1.12×10^{10}	1546.0	5.36×10^{6}
Fat	4.18	4.74×10^{8}	920.0	1.35×10^{6}

Figures

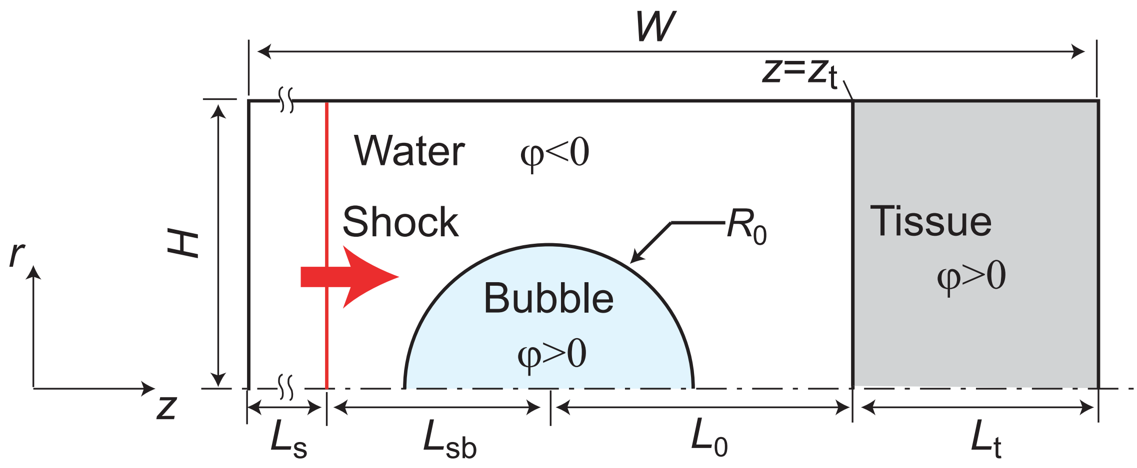

Figure 1. Schematic of present simulation.

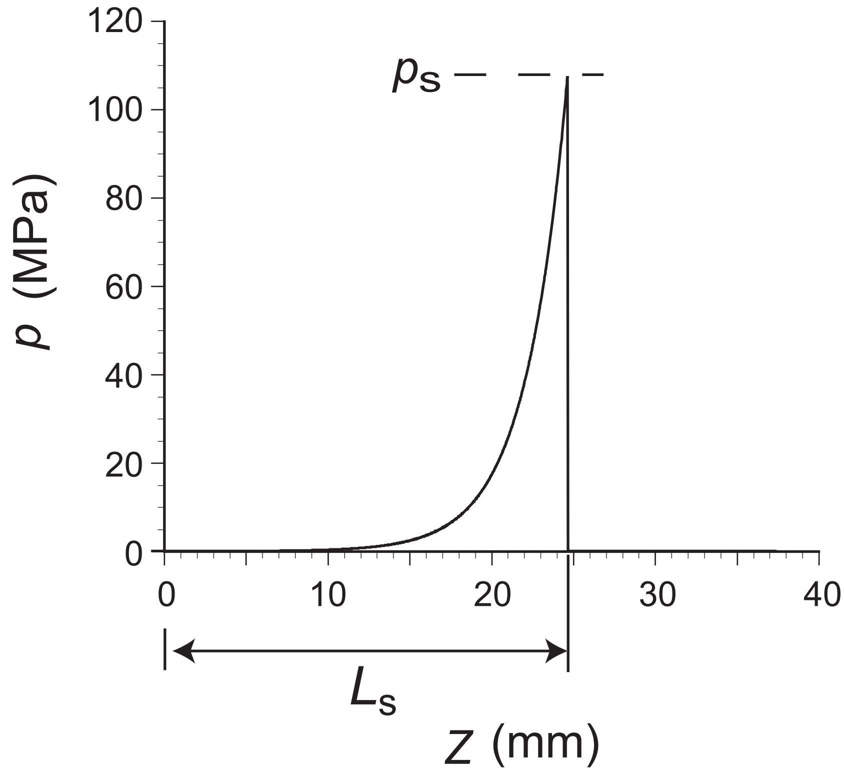

Figure 2. Incident shock wave profiles. The profile was obtained from the experimental data in Kodama and Takayama (1998).

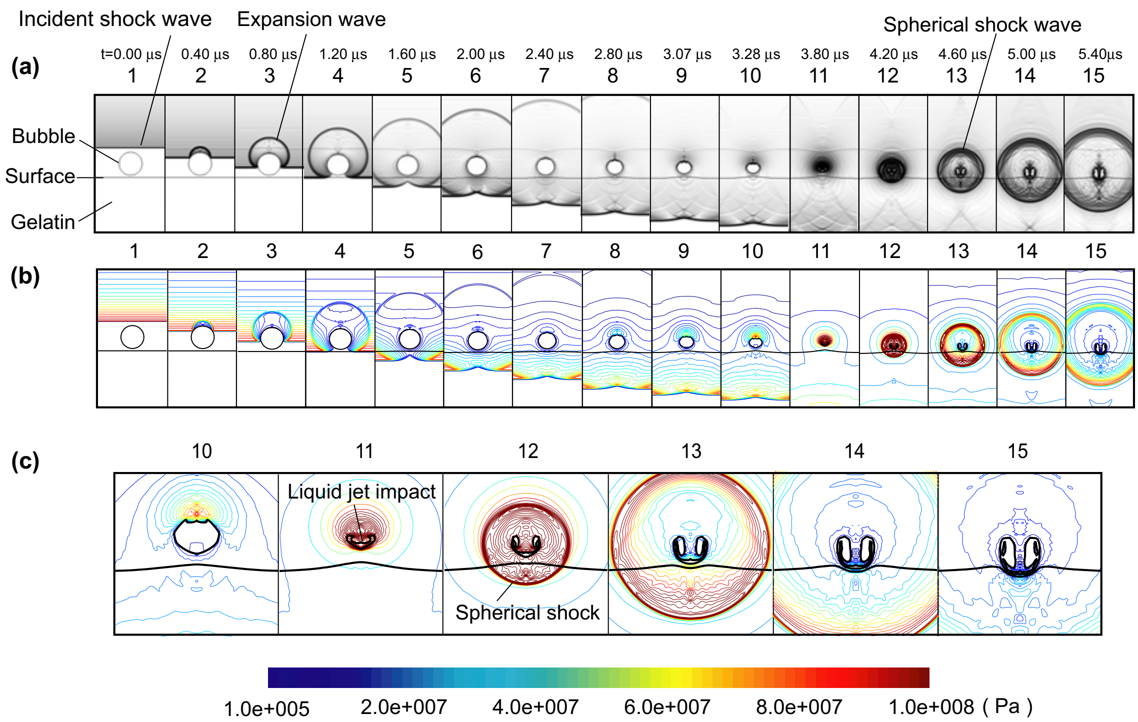

Figure 3. Bubble collapse near gelatin at $L_0/R_0 = 1.2$: (a) schlieren images; (b) pressure contours; (c) enlarged figures for (b).

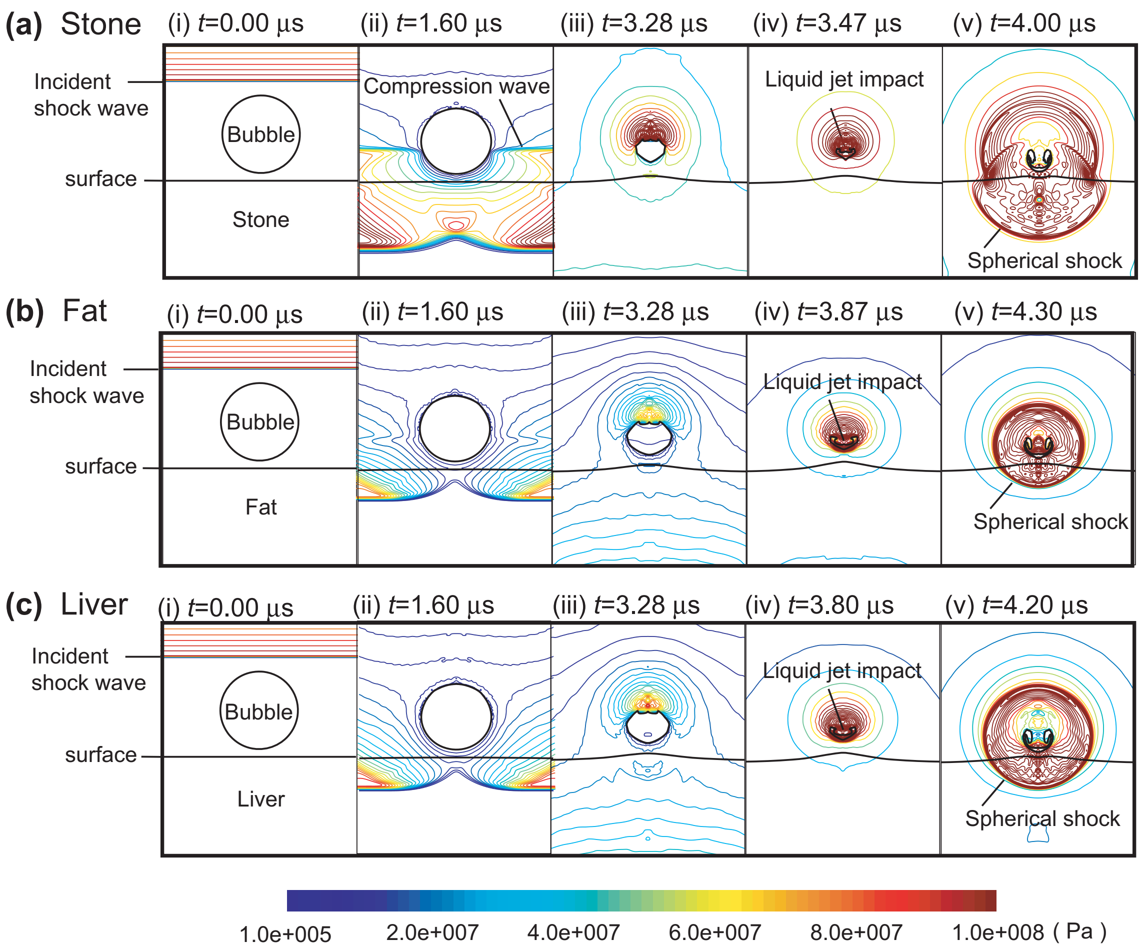

Figure 4. Bubble collapse near stone, fat, and liver boundaries at $L_0/R_0 = 1.2$: (a) near stone; (b) near fat; (c) near liver.

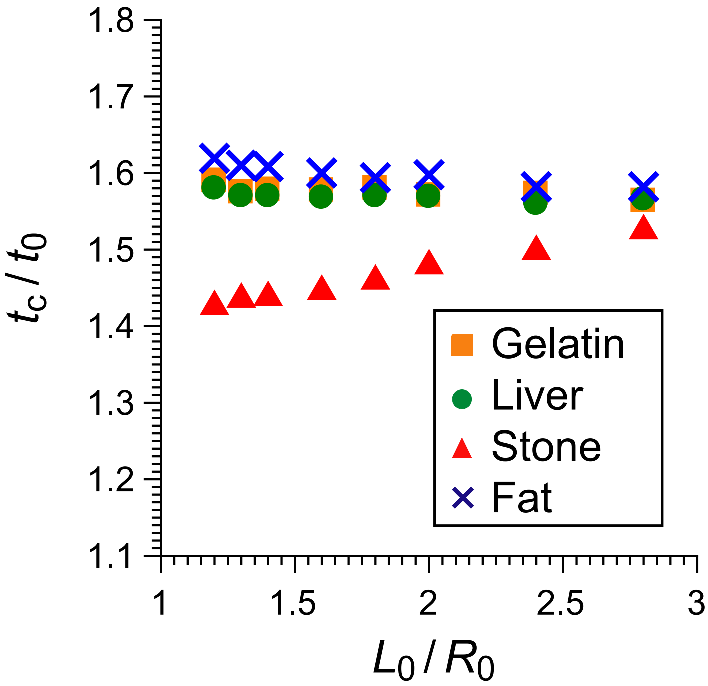

Figure 5. Bubble collapse time versus L_0/R_0.

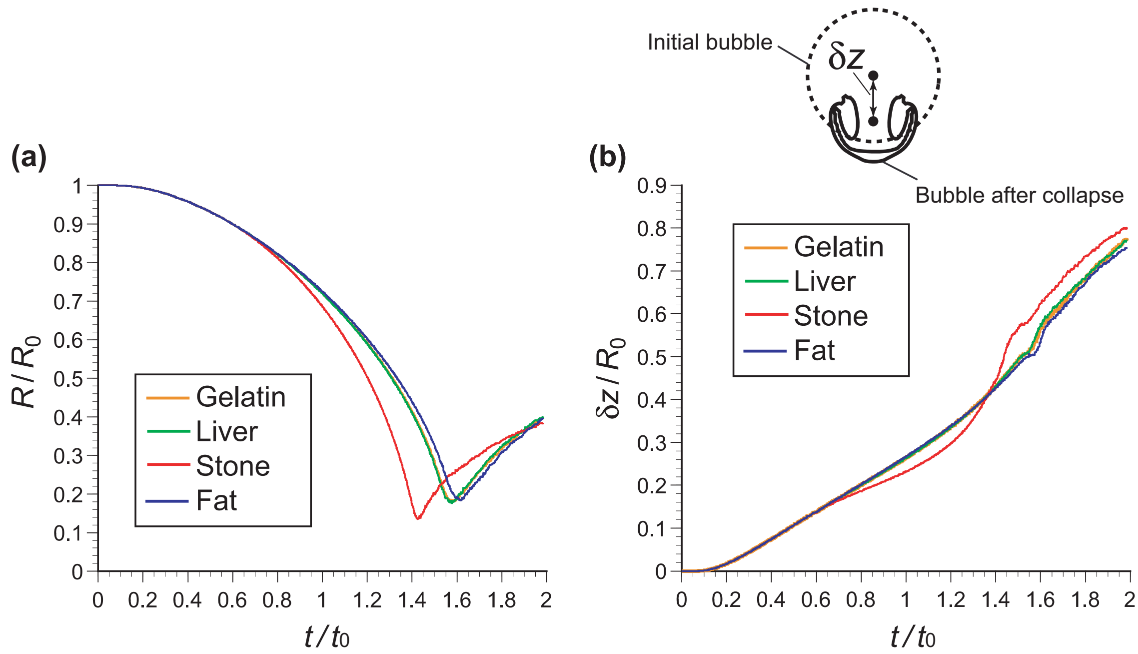

Figure 6. Bubble radius and translational motion of bubble at L_0/R_0 = 1.2: (a) bubble radii; (b) trajectories of the bubble centroid.

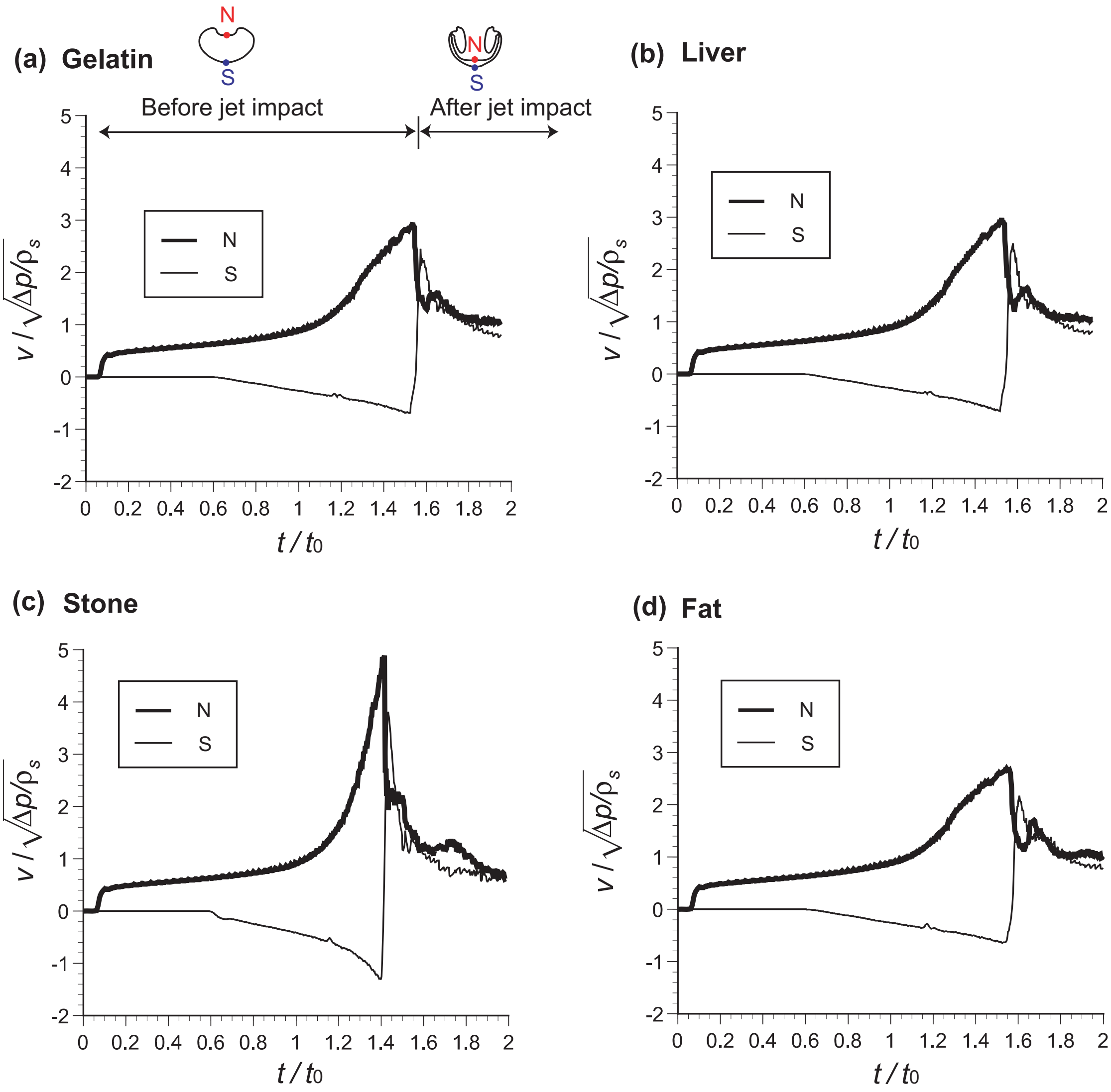

Figure 7. Liquid jet velocities of bubble near each tissue material at $L_0/R_0 = 1.2$.

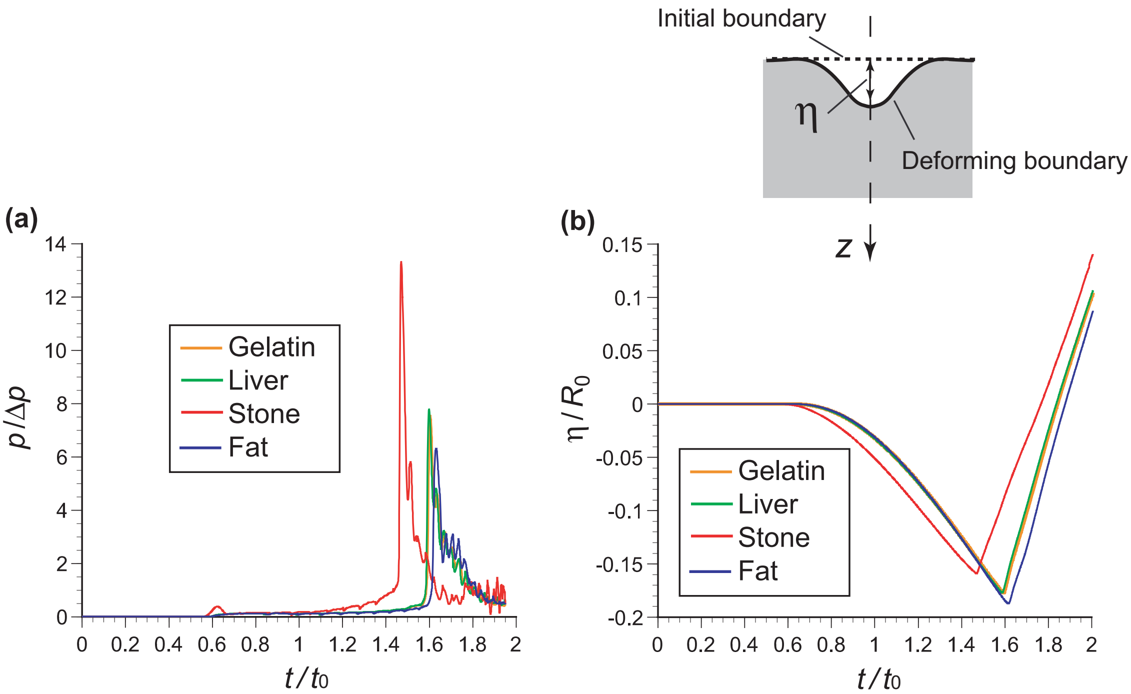

Figure 8. Time histories of pressure at tissue boundary and its deformation at L_0/R_0 = 1.2: (a) pressure at the boundary; (b) displacement of the boundary.

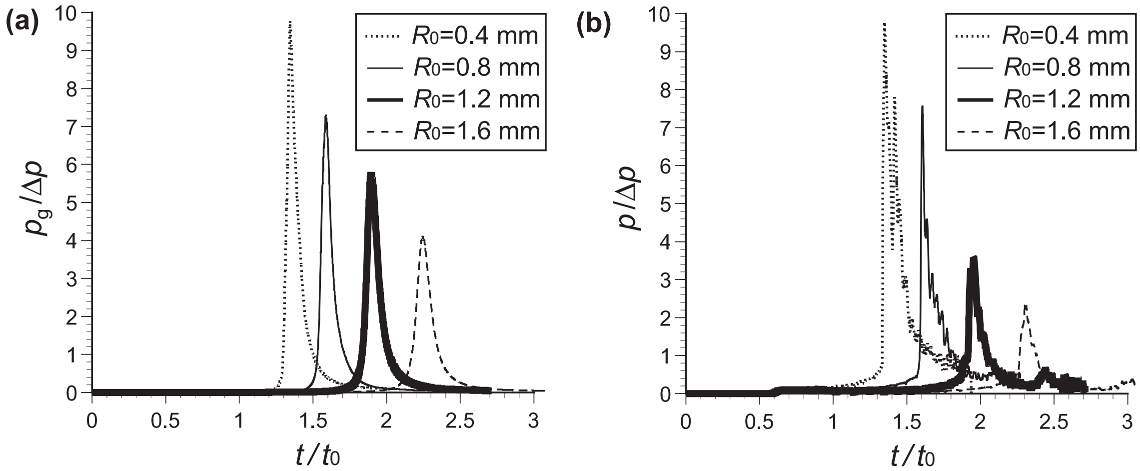

Figure 9. Time histories of average pressure inside bubble and pressure at gelatin boundary for L_0/R_0 = 1.2: (a) average pressure of air inside bubble; (b) pressure at gelatin boundary.

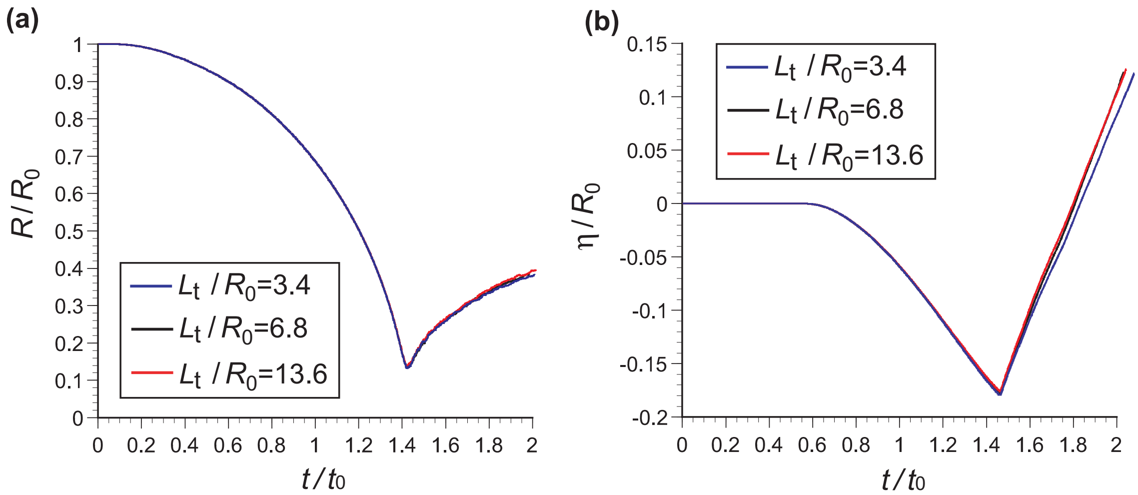

Figure 10. Time histories of bubble radius and displacement of stone boundary for L_t/R_0 = 3.4, 6.8, and 13.6: (a) bubble radius; (b) displacement of stone boundary.

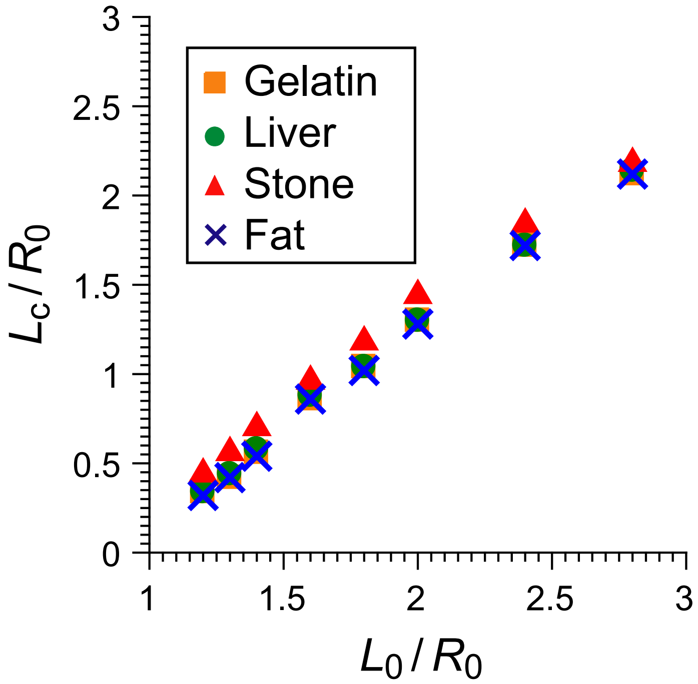

Figure 11. Bubble collapse position for L_0/R_0.

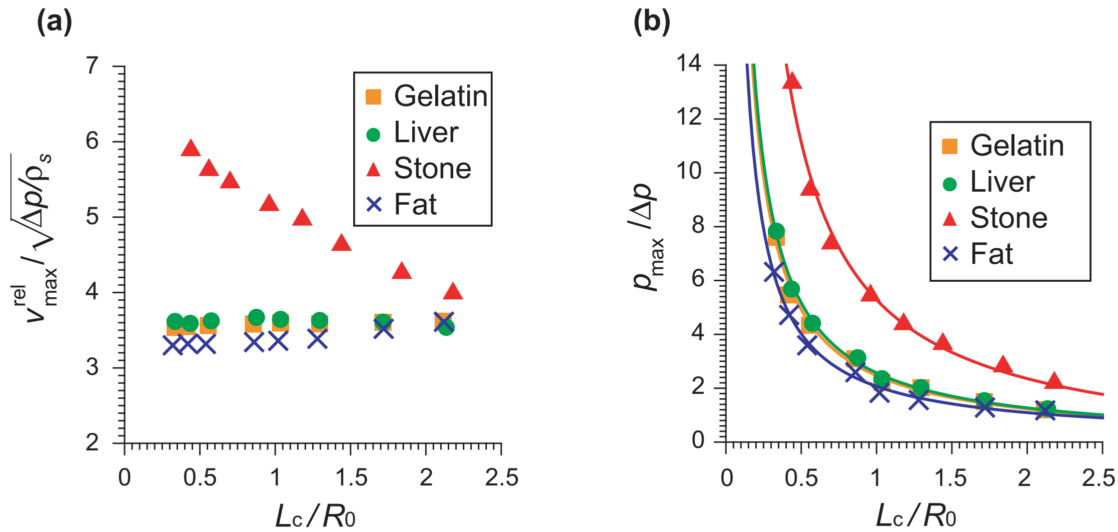

Figure 12. Maximum liquid jet velocity and the maximum pressure at tissue boundary: (a) maximum jet velocity versus L_c/R_0; (b) maximum pressure at tissue boundary versus L_c/R_0.

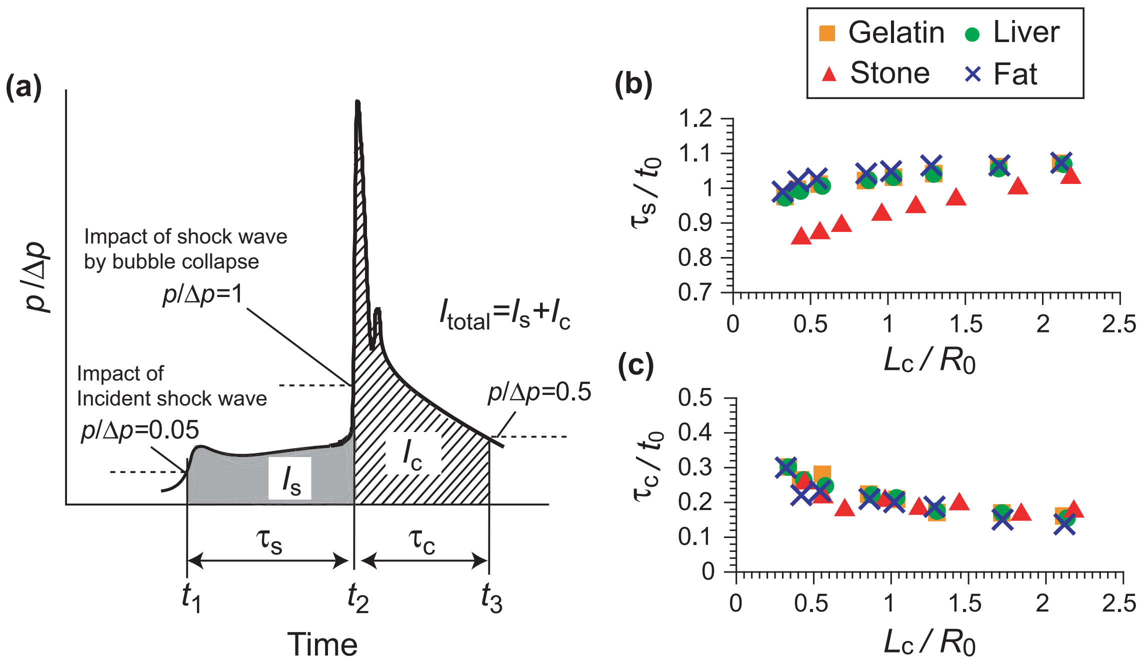

Figure 13. Definition of impulse and duration time of impulse: (a) schematic of evaluation method of impulse; (b) duration times τ_s versus L_c/R_0; (c) duration times τ_c versus L_c/R_0.

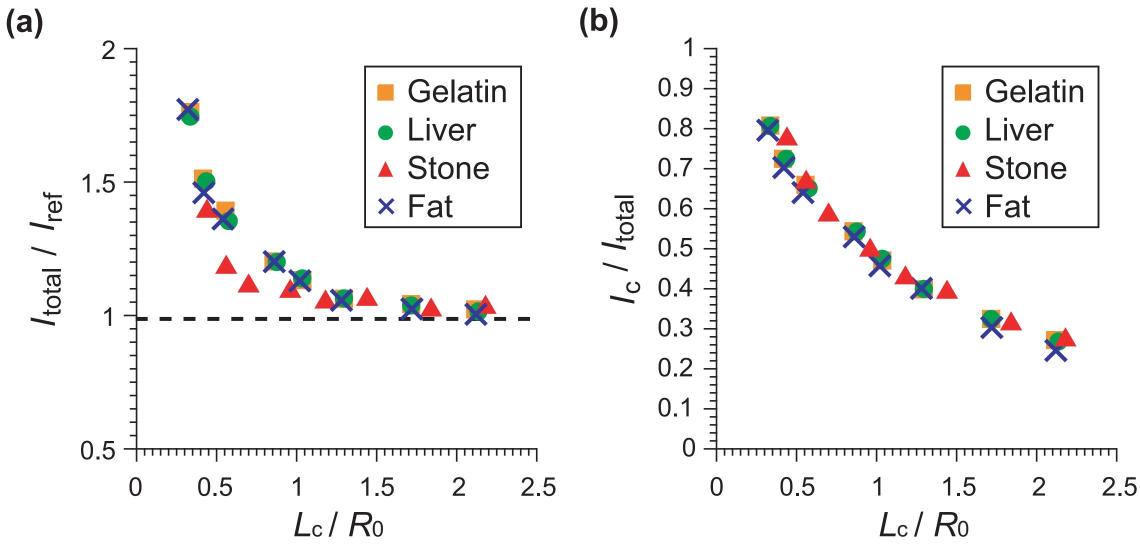

Figure 14. Impulse at each tissue boundary: (a) total impulse for each tissue versus L_c/R_0; (b) fraction of impulse caused by bubble collapse I_c/I_{total} versus L_c/R_0.

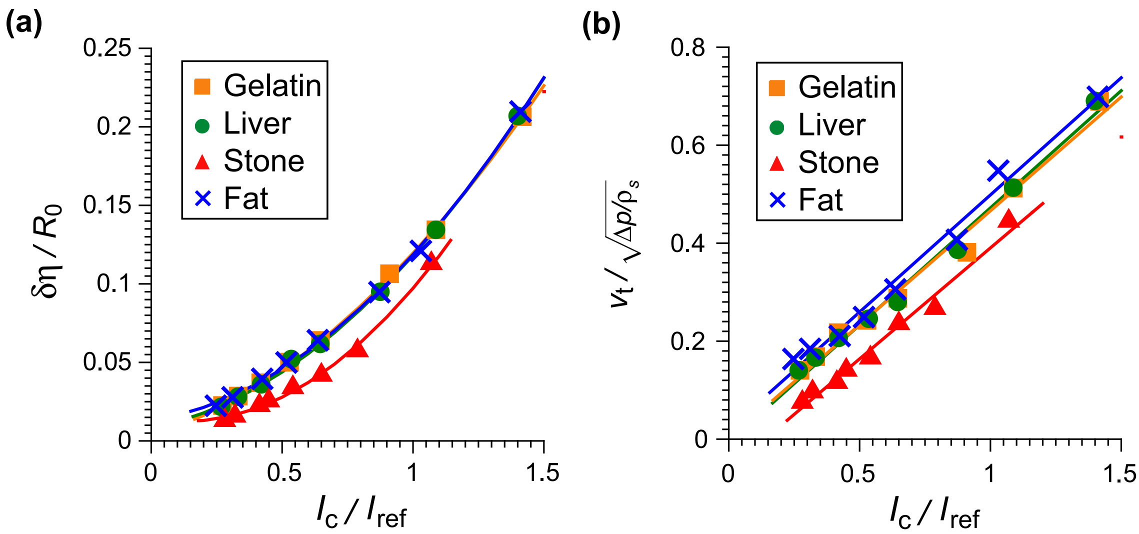

Figure 15. Displacement of tissue boundary and tissue boundary velocity as a result of bubble collapse: (a) displacement of tissue boundary versus I_c/I_{ref}; (b) tissue boundary velocity versus I_c/I_{ref}.